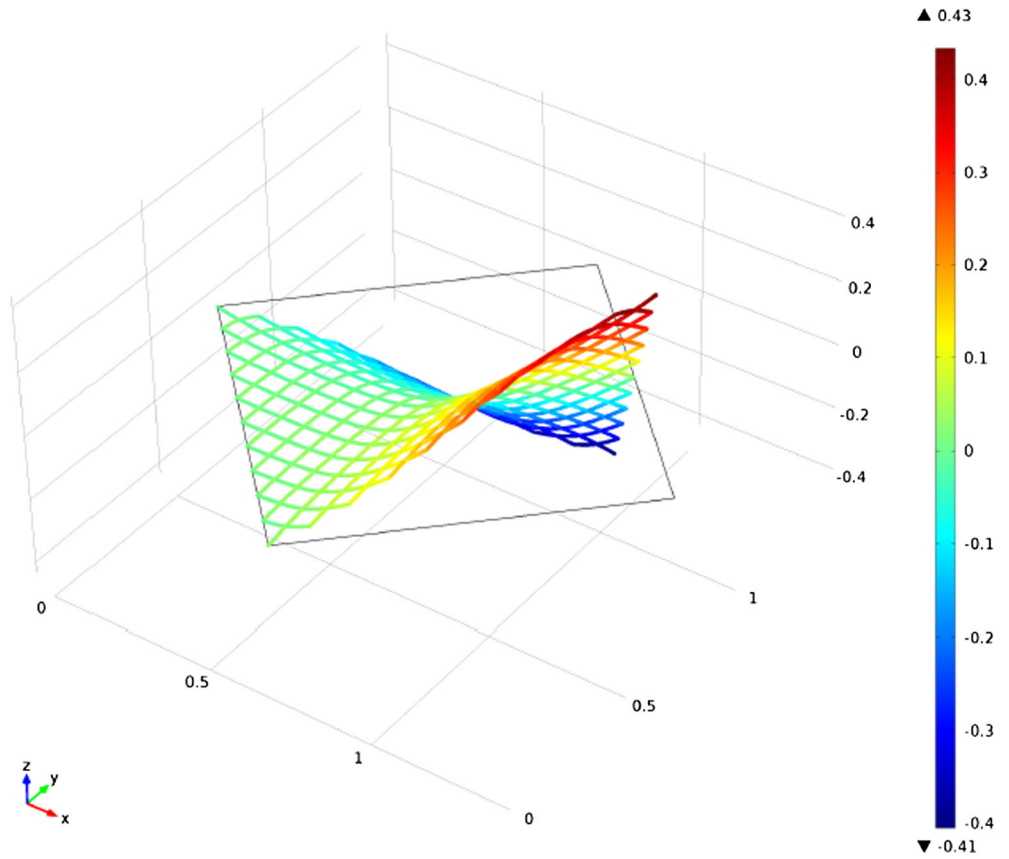

Fig. 21 Numerical simulation of torsion of a square sheet ($\theta = 60°$) using the elastic surface model presented above. Colors represent qualitatively the out-of-plane component of the displacement u_3 (color figure online)

Furthermore, a strain energy density function, which depends on the first and second gradients of the deformation and incorporating the orthotropic symmetry conferred by the reference fiber arrangement, can be proposed [47]

$$W = w(\lambda, \mu, J) + \frac{1}{2}\left(A_1|g_1|^2 + A_2|g_2|^2 + A_\Gamma|\boldsymbol{\Gamma}|^2 + k_1K_1^2 + k_2K_2^2 + k_TK_T^2\right) \tag{27}$$

where $A_1,\ A_2,\ A_\Gamma,\ k_1,\ k_2,\ k_T$ are constitutive constants. In Fig. 21, numerical simulations of the torsion of a square sheet using the elastic surface model presented above are shown. Many fiber reference curvatures have been considered (e.g., sinusoidal, spiral, parabolic fibers), and for parabolic fibers, experiments (Fig. 22) and model (Fig. 23) both show that, after a critical load, out-of-plane buckling occurs during bias extension, because the transverse (curved) beams in the middle of the specimen undergo buckling induced by the shortening of the middle width of the specimen.

A 2D continuum model embedded in a 3D space has been also proposed [48] where, relying on a variational framework, the following strain energy density is proposed

$$\begin{aligned}\pi = \frac{1}{2}\Big\{ & K_e\left[\left(\epsilon^1\right)^2 + \left(\epsilon^2\right)^2\right] + K_s\gamma^2 + \\ & + K_t\left[\left(\kappa_1^1\right)^2 + \left(\kappa_1^2\right)^2\right] + K_n\left[\left(\kappa_2^1\right)^2 + \left(\kappa_2^2\right)^2\right] + K_g\left[\left(\kappa_3^1\right)^2 + \left(\kappa_3^2\right)^2\right]\Big\}\end{aligned} \tag{28}$$

It corresponds to a system of two orthogonal continuous families "1" and "2" of straight shear-undeformable beams arranged along the coordinate axes in the reference configuration and resembling the pantographic microstructure. The fibers of family α are parallel to the direction $\hat{e}_\alpha$. The contributions $\frac{1}{2}K_e\left(\epsilon^1\right)^2$ and

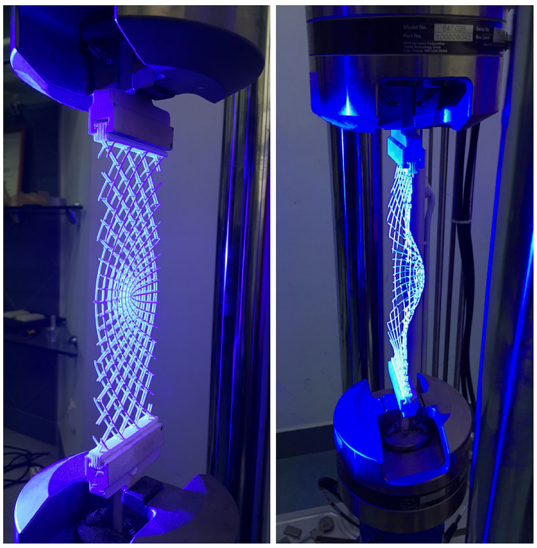

Fig. 22 Bias extension test on parabolic pantographic fabric. Out-of-plane buckling is observed after critical loading

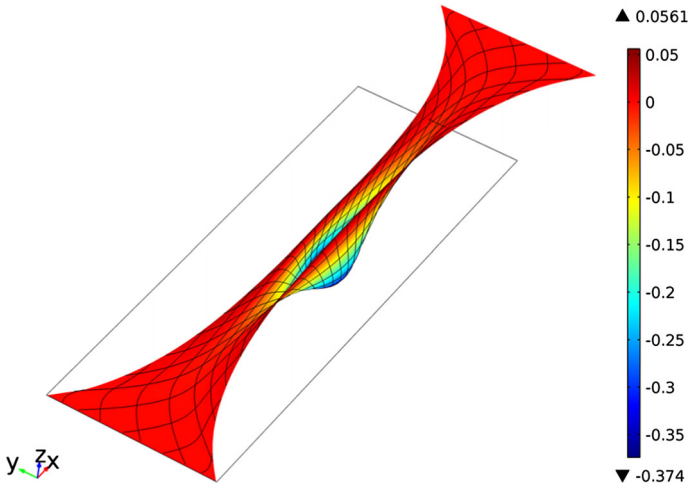

Fig. 23 Simulation of bias extension test on parabolic pantographic fabrics. Out-of-plane buckling is observed after a critical loading. Deformed configuration and qualitative out of plane displacement

$\frac{1}{2}K_e\left(\epsilon^2\right)^2$ stand for the elongation of fibers belonging to, respectively, the families "1" and "2." The strain measure $\boldsymbol{\epsilon}^\alpha$, with $\alpha = 1, 2$, is defined as

$$\epsilon^\alpha = \left\| \frac{\partial \chi}{\partial X_\alpha} \right\| - 1 \tag{29}$$

and $K_e \in [0, \infty)$ is the corresponding stiffness, which is assumed to be the same for both families of fibers. The contribution $K_s\gamma^2$ is accounting for the shear deformation of the sheet, i.e., it is due to the relative rotation of two orthogonal intersecting fibers. It represents the strain energy stored in the pivot because of its torsion of angle γ. The strain measure $\gamma \in [-\frac{\pi}{2}, \frac{\pi}{2}]$, also referred to as the shear angle, is expressed as

$$\gamma = \arcsin \frac{\frac{\partial \chi}{\partial X_1} \cdot \frac{\partial \chi}{\partial X_2}}{\left\| \frac{\partial \chi}{\partial X_1} \right\| \left\| \frac{\partial \chi}{\partial X_2} \right\|} \tag{30}$$

and $K_s$is a positive constitutive parameter. The terms $\frac{1}{2}\left[K_t\left(\kappa_1^1\right)^2 + K_n\left(\kappa_2^1\right)^2 + K_g\left(\kappa_3^1\right)^2\right]$ and $\frac{1}{2}\left[K_t\left(\kappa_1^2\right)^2 + K_n\left(\kappa_2^2\right)^2 + K_g\left(\kappa_3^2\right)^2\right]$ are due to twist, normal bending and geodesic bending of beams belonging, respec-

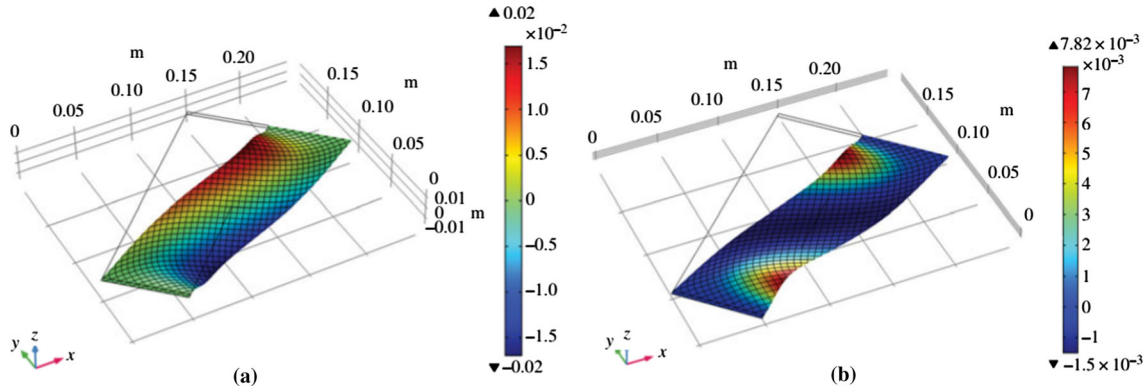

Fig. 24 Shear test. Qualitative buckled shapes of the first two bifurcation modes. Colors indicate values of the out-of-plane displacement. **a** First and **b** second buckling modes (color figure online)

tively, to families "1" and "2" of fibers. The strain measures $\kappa_1^\alpha, \kappa_2^\alpha, \kappa_3^\alpha$ are the coordinates, in the augmented levorotatory reference Cartesian frame, of the axial vector corresponding to the skew tensor $W^\alpha = (R^\alpha)^{\mathrm{T}} \frac{\partial R^\alpha}{\partial X_\alpha}$, which is the so-called current curvature tensor. The orthogonal tensor R^α transforms the augmented levorotatory reference Cartesian frame vectors into the following ordered triplet: (1) the unitary vector tangent to the deformed coordinate line α; (2) the unitary vector normal to the previous one and lying in the plane tangent to the deformed surface; (3) the unitary vector normal to the plane tangent to the deformed surface. Explicit (lengthy) derivations can be found in Ref. [48].

It is worth noting that (1) since the beams are assumed to be shear-undeformable (2) both R^1 and R^2 transform the third vector $\hat{e}_3$ of the augmented levorotatory reference Cartesian frame into the same vector, (3) assuming that principal inertia axes of the cross sections for the two families "1" and "2" of beams in the undeformed configuration are considered to be, respectively, $(\hat{e}_2, \hat{e}_3)$ and $(-\hat{e}_1, \hat{e}_3)$, the cross sections of the beams belonging to the two families "1" and "2" are eigen-inertia vectors in the deformed configuration the unitary vectors of points (2) and (3) above and, hence, they share the second principal inertia axis at point (3) above. Such vector is also interpreted as the current axis of the elastic cylindrical pivot. This means that deformation modes of the pivots other than their torsion are kinematically excluded in this model, i.e., the pivots are assumed to remain orthogonal to both fibers in the current configuration and only their torsion contributes to the strain energy. Further, κ_1^α, κ_2^α, κ_3^α can also be interpreted as geodesic torsion, normal curvature and geodesic curvature of the deformed surface multiplied, respectively, by $\| \frac{\partial \chi}{\partial X_\alpha} \|$, since X_α is not a unitary speed parameterization. Last, the fibers intersecting in one point cannot detach or have a relative displacement, since their motion is described by the same placement function. (This is not a so-called mixture model.) Using the above model, shear test simulations have been performed reporting the occurrence of out-of-plane buckling (Fig. 24).

1.7 Analytical identification of elastic plate models

Let us consider a two-dimensional body, whose points can be put in a bijective correspondence with a closed subset $\mathcal{B}$ of the Euclidean space $\mathbb{R}^2$. The set $\mathcal{B}$ represents the shape of the body in the reference (undeformed) configuration. A Cartesian coordinate system $(\mathcal{O}, (\hat{e}_1, \hat{e}_2))$ is introduced, with $X = (X_1, X_2)$ the coordinates of the generic point in the Euclidean space $\mathbb{R}^2$.

Working in a Lagrangian framework, a placement function $\chi : \mathcal{B}_0 \to \mathbb{R}^2$ such that the image $x = \chi(X)$ of X through χ is the current position of point X. The displacement field $u : \mathcal{B}_0 \to \mathbb{R}^2$ is defined as $u(X) = \chi(X) - X$. The placement, or equivalently the displacement, is the independent kinematic descriptor of the system. The image $\mathcal{B} = \chi(\mathcal{B})$ of $\mathcal{B}$ through χ is the current shape of the body. Let $F = \nabla_X \chi$ be the gradient (with respect to the Lagrangian coordinate X) of the placement function χ. The tensor F belongs to Lin^+, the group of second order tensors with positive determinant, i.e., orientation preserving. An objective strain measure $G = \left[F^T F - I\right]/2$ (Green-Lagrange strain tensor) is then defined. Henceforth, the subscript X will be omitted in ∇_X and each space derivative will be considered a material derivative. When the strain

energy density $\hat{U}(G, \nabla G)$ is considered to be depending quadratically upon the deformation tensor G and its gradient ∇G, the following representation formula applies [49]

$$\hat{U}^{\text{strain}} = \frac{1}{2}\epsilon^T C_{3\times 3}\epsilon + \frac{1}{2}\eta^T A_{6\times 6}\eta \tag{31}$$

with

$$\epsilon = \left(G_{11}\ G_{22}\ \sqrt{2}G_{12}\right)^{\mathrm{T}} \tag{32}$$

and

$$\eta = \left(G_{11,1}\ G_{22,1}\ \sqrt{2}G_{12,2}\ G_{22,2}\ G_{11,2}\ \sqrt{2}G_{12,1}\right)^{\mathrm{T}} \tag{33}$$

In order to account for anisotropy of the material, we must assume invariance of the strain energy density under the action, on the Cartesian coordinate system $\mathcal{O}, (\hat{e}_1, \hat{e}_2)$ labeling points of the reference configuration, of some symmetry group S of transformations, which could be any subgroup of *Orth*. When the symmetry group is the dihedral group D4 (orthotropic material), the representations for the matrices $C_{3\times 3}$ and $A_{6\times 6}$ read

$$C^{D4}_{3\times 3} = \begin{pmatrix} c_{11} & c_{12} & 0 \\ c_{12} & c_{22} & 0 \\ 0 & 0 & c_{33} \end{pmatrix} \tag{34}$$

and

$$A^{D4}_{6\times 6} = \begin{pmatrix} A^{D4}_{3\times 3} & 0 \\ 0 & A^{D4}_{3\times 3} \end{pmatrix} \tag{35}$$

with c_{11} and c_{12} in $C^{D4}_{3\times 3}$ corresponding to the two Lamé coefficients

$$A^{D4}_{3\times 3} = \begin{pmatrix} a_{11} & a_{12} & a_{13} \\ a_{12} & a_{22} & a_{23} \\ a_{13} & a_{23} & a_{33} \end{pmatrix} \tag{36}$$

In Refs. [50–52], compatible identifications of the constitutive parameters appearing in Eq. (31) have been carried out, thus completely characterizing the set of constitutive parameters in terms of the fiber base material parameters (i.e., Young's modulus), of the fiber cross section parameters (i.e., area and moment of inertia), and of the distance between the nearest pivots. In particular, the constitutive parameters have been identified in the small strain case $|\nabla u| \ll 1$, modeling fibers as (geometrically linear) Euler–Bernoulli beams and pivots as rotational (elastic) springs with a quadratic potential in the relative rotation (torsion of pivots) angle between fibers belonging to two different families. The following expressions for the matrices $C^{D4}_{3\times 3}$ and $A^{D4}_{3\times 3}$ are the outcome of the investigation [52]

$$C^{D4}_{3\times 3} = \begin{pmatrix} \frac{EA}{d} & 0 & 0 \\ 0 & \frac{EA}{d} & 0 \\ 0 & 0 & 2k_R \end{pmatrix} \tag{37}$$

$$A^{D4}_{3\times 3} = \frac{EI}{d}\begin{pmatrix} 0 & 0 & 0 \\ 0 & 1 & -\sqrt{2} \\ 0 & -\sqrt{2} & 2 \end{pmatrix} \tag{38}$$

with E, A and I being, respectively, the Young's modulus, the cross-sectional area and the inertia moment of the cross section of beams, and d being the spacing between adjacent beams. Finally, k_R is the equivalent elastic torsional stiffness of the cylindrical pivots. The shear strain relative to the directions v and w is defined as (with $-\frac{\pi}{2} < \gamma < \frac{\pi}{2}$)

$$\sin\gamma = \cos\left(\frac{\pi}{2} - \gamma\right) = \frac{Fv \cdot Fw}{\|Fv\|\ \|Fw\|} = \frac{w^T F^T F v}{\|Fv\|\ \|Fw\|} = \frac{w^T\ (2G + I)\ v}{\|Fv\|\ \|Fw\|}. \tag{39}$$

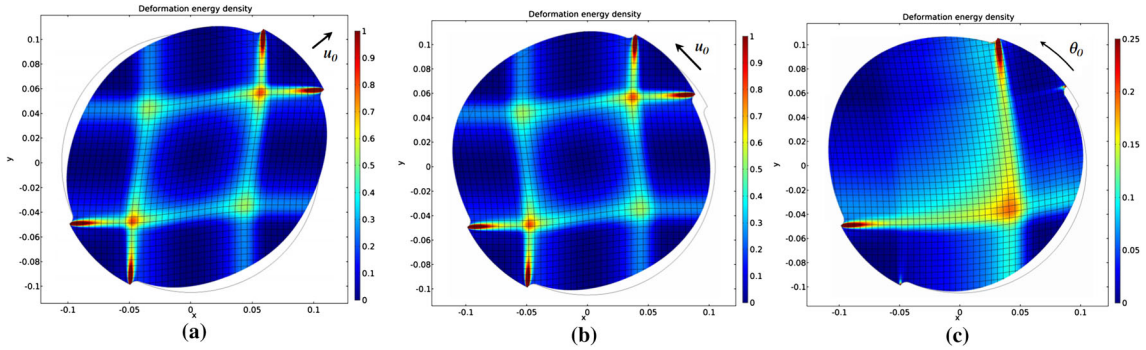

Fig. 25 Circular pantographic specimen. Qualitative color maps of the strain energy density for: bias extension test (**a**), shear test (**b**), rotation test (**c**)

In the present case $w = \hat{e}_1$ and $v = \hat{e}_2$. Thus, assuming that $-\frac{\pi}{2} \leq \gamma \leq \frac{\pi}{2}$

$$\gamma = \arcsin\left(\frac{2G_{12}}{\sqrt{\left(1+u_{1,1}\right)^2 + u_{2,1}^2}\sqrt{\left(1+u_{2,2}\right)^2 + u_{1,2}^2}}\right). \tag{40}$$

In the case of small strains, i.e., geometrically linear case $|\nabla u| \ll 1$

$$\gamma \simeq \arcsin\left(u_{1,2} + u_{2,1}\right) \simeq u_{1,2} + u_{2,1}. \tag{41}$$

Equation (31) yields the following remarkable expression for the strain energy density

$$\hat{U}^{\text{strain}} = \underbrace{\frac{1}{2}k_R\left(u_{1,2}+u_{2,1}\right)^2}_{\text{shear (pivot torsion) contribution}} + \underbrace{\frac{EA}{2d}\left(u_{1,1}^2+u_{2,2}^2\right)}_{\text{extension of fibers}} + \underbrace{\frac{EI}{2d}\left(u_{1,22}^2+u_{2,11}^2\right)}_{\text{bending of fibers}} \tag{42}$$

In Ref. [50], numerical solutions using the strain energy density (42) are presented for a circular pantographic specimen and three exemplary problems: bias extension, shear, and rotation tests (Fig. 25).

In Ref. [53], two pantographic sheets with an aspect ratio 3:1 are considered, having (1) the same fiber directions and (2) a part of their common sides interconnected by terminal clamping constraints, i.e., the displacements in the interconnected regions are pointwise equal for the two pantographic sheets. In the region corresponding to the cut separating the two sheets, no kinematic constraint is assumed for their relative displacement and the results shown in Fig. 26 are obtained for a standard bias extension test. Pantographic sheets without any internal cut are considered as well, see Fig. 27, where Eulerian representations of the strain energy densities are given for two nonstandard bias extension tests and in presence (absence) of the shear energy contribution. In particular in the first (higher) two plots in Fig. 27 the left side of the specimen have been clamped and the other sides are free, while the vertices of the right side are displaced along the direction of the longer sides. Instead, in the lower two plots, the left side of the specimen has been clamped and the lower half of the right side has been displaced along the direction of the longer sides, while the remaining boundaries are free. Second gradient energies allow for external actions on 2D continua not only on edges, but also on vertices, as vertex boundary conditions and vertex-forces.

1.8 Wave propagation in discrete arrangements of Euler beams

In Ref. [54], a model for studying the dynamics of pantographic fabrics has been introduced and subsequently employed [55,56]. Pantographic rectangular "long" waveguides are studied and time-dependent boundary displacements inducing the onset of traveling waves are considered. In this model, the two families of orthogonal fibers are regarded as two families of $1D$ orthogonal straight continua arranged in a rectangle in the reference configuration. Each continuum $\mathcal{C}_i$ has a standard linearized Euler elastic potential given by

$$U_i = \frac{1}{2}\int_{\mathcal{C}_i} k_M\left(u''(s)\right)^2 + k_N\left(w'(s)\right)^2 \mathrm{d}s \tag{43}$$

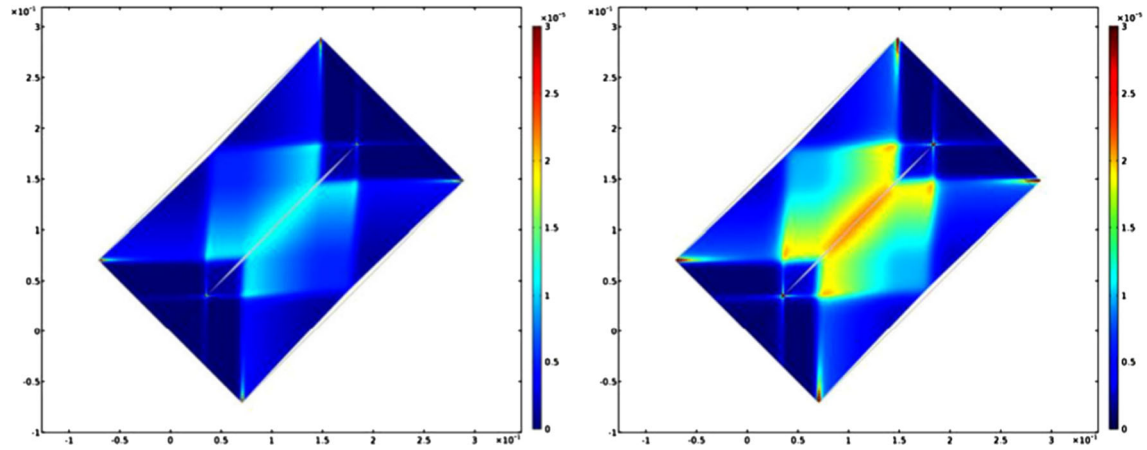

Fig. 26 Effect of a cut inside a sheet. Eulerian representation of the elastically stored energy density for a sheet with lower shear stiffness (left) and for a sheet with higher shear stiffness (right), both subject to a standard bias extension test

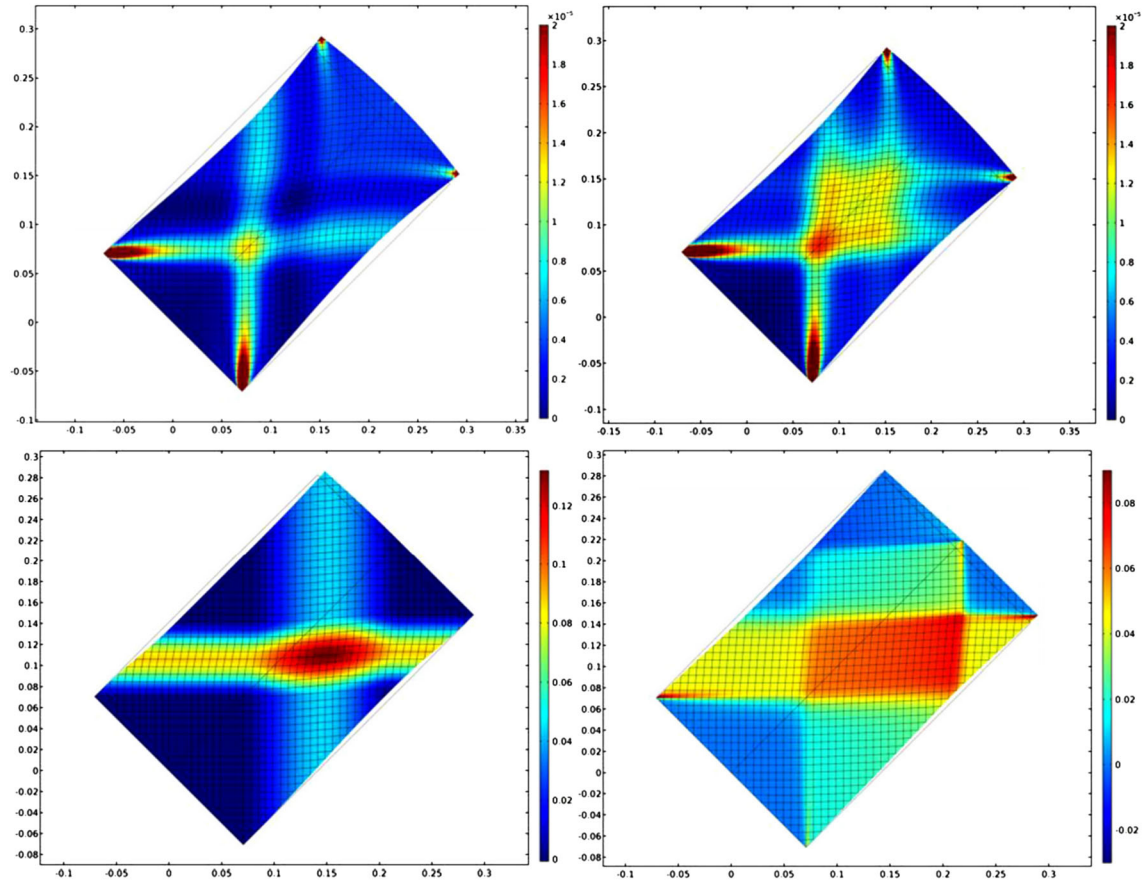

Fig. 27 Nonstandard bias extension test: Eulerian representation (including deformed shape and deformed sampled material lines) of the strain energy density for a sheet whose expression does not include the shear contribution (left) and for a sheet whose strain energy includes the shear contribution (right)

with s an abscissa introduced on each $\mathcal{C}_i$, k_M the bending stiffness, k_N the axial stiffness, u and w, respectively, the transverse and axial displacements. Dots in Fig. 28 (left) indicate the presence of frictionless hinges that do not interrupt the continuity of the beams. The displacement prescribed on the structure is an impulse function $\mathfrak{I} = u_0 * \operatorname{sech}[\tau(t - t_0)]$, with τ being a parameter affecting the duration of the pulse [Fig. 28 (right)].

In Fig. 29 (left) plots of the deformed shape of a pantographic strip during the propagation of a wave generated by a vertical impulse, uniformly applied on the upper side of the specimen while its lower side

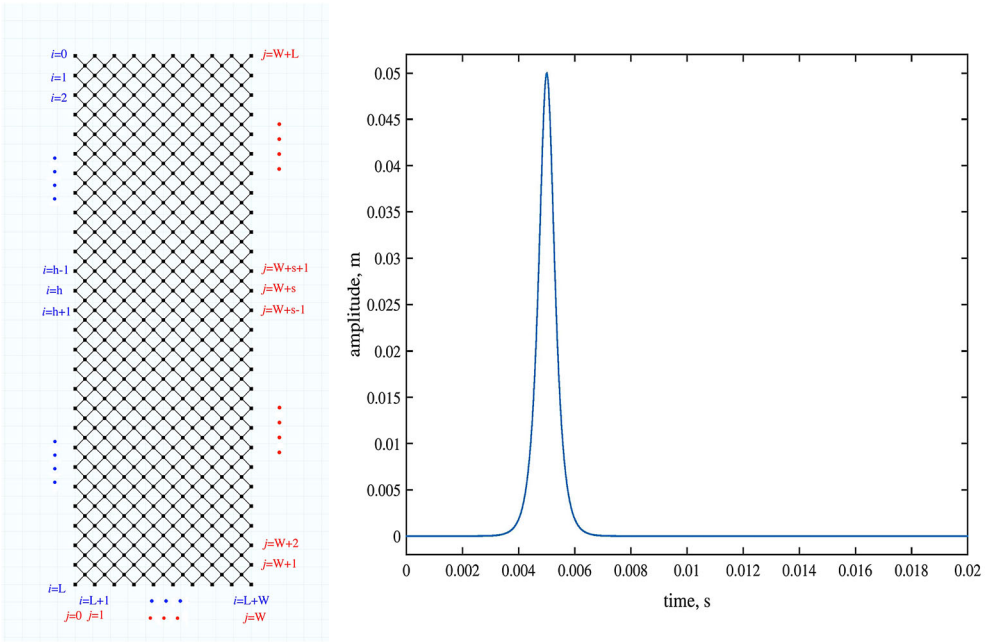

Fig. 28 Reference configuration (left) and time history of the impulse (right)

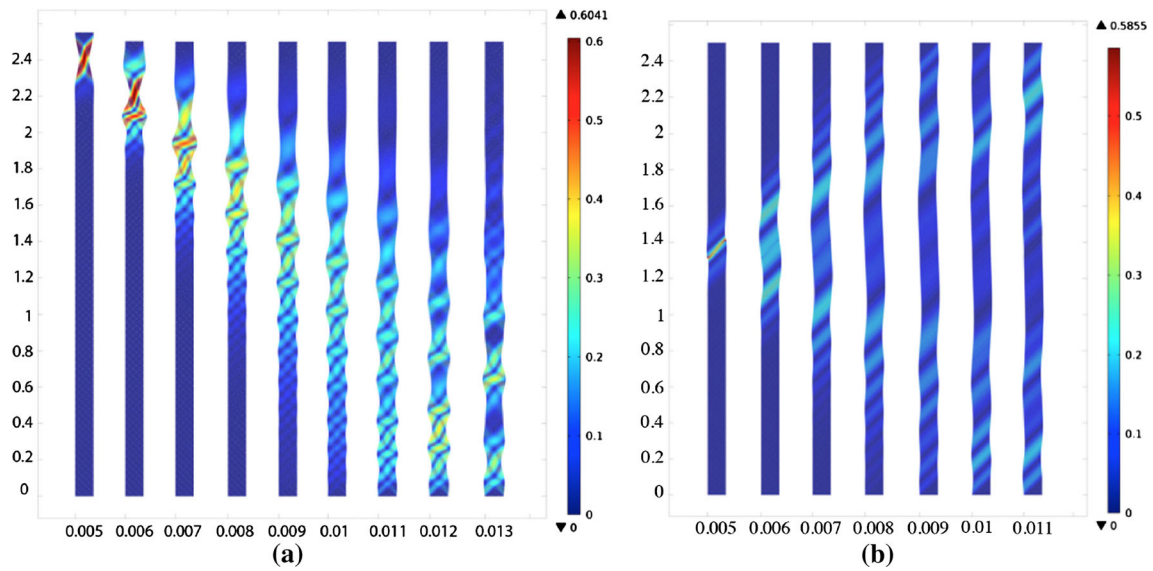

Fig. 29 Qualitative displacement plot of a wave propagating after a prescribed vertical displacement on the upper side (left). Wave propagating after double impulse (right)

remains clamped, are shown. Colors represent the magnitude of the total rotation of the cross section of the beams. In Fig. 29 (right), plots of the deformed shape of a pantographic strip during the propagation of a wave, generated by a double impulse applied at the middle height of the specimen, are shown, along with colors representing the magnitude of the total rotation of the cross section of the beams. By double impulse, we mean a couple of displacements, having the same orientation but opposite directions, oriented in one of the two orthogonal characteristic directions of the pantographic sheet. Such displacements are prescribed on two points at the opposite ends of two adjacent beams, i.e., consecutive beams belonging to the same orthogonal family of $1D$ continua, and their amplitude over time is shown in Fig. 28.

Such a double impulse corresponds, in the continuous homogenized limit case, to a double force, i.e., to a pair of forces with null resultant and moment. Figure 30 shows that the energy of the system remains

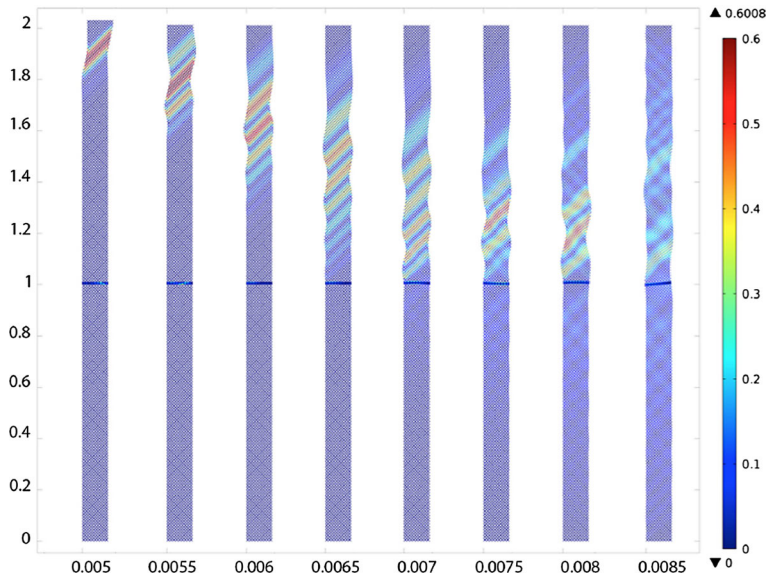

Fig. 30 Qualitative displacement of wave propagation in two identical lattices connected by an array of vertical beams

substantially confined in the upper half of the waveguide and propagation of waves beyond the discontinuity is negligible. Therefore, such type of discontinued pantographic structures induces damping.

2 Damage and failure in pantographic fabrics

So far the study of damage mechanisms in pantographic fabrics has been addressed from a modeling standpoint [57,58]. Further experimental data can be found [10,59]. In Ref. [57], in the aforementioned discrete quasi-static Hencky spring model (Sect. 1.3) a simple irreversible rupture mechanisms is considered for the springs. A spring is ruptured if its strain level exceeds (upper threshold) or is less than (lower threshold) a certain (constant) threshold. In particular, the criterion for rupture of a spring at iteration t, which discriminates whether that spring has to be removed from the computations at iteration $t+1$ or not, is based on (constant) thresholds for the relative elongation of extensional springs, e.g., $(\|p_{i+1,j} - p_{i,j}\| - \epsilon)$ (upper and lower thresholds are employed for this deformation measure). Upper thresholds for the relative rotation of adjacent springs belonging to the same fiber like, e.g., $(\cos\vartheta^1_{i,j} + 1)$ and for the relative rotation of adjacent springs belonging to different fibers like $|\vartheta^3_{i,j} - \frac{\pi}{2}|$ are contemplated but are not considered. Since the analyzed pantographic sheet is made out of a ductile material (polyamide), damage is governed by fiber breakage due to excessive extension rather than fiber breakage due to excessive bending or pivot failure due to torsion.

An experimental evidence [10] is provided by displacement-controlled uniaxial bias extension tests (Fig. 31) when performed on three different polyamide specimens. The first failure event was observed at the corners of the specimen, where the elongation of fibers is the highest.

This evidence is confirmed, through a different test [57] (see Fig. 32), since fiber elongation is the highest at the lower-left and upper-right corners. When the sample is made out of a brittle material, damage is governed by excessive shear strains (i.e., torsion of pivots) that, in the displacement-controlled uniaxial bias extension test, reaches its maximum near the two internal vertices of the quasi-rigidly deforming triangles.

In Ref. [57], a slow-rate (15 mm/min) of uniform horizontal displacement on the top of the specimen is prescribed. From the prescribed horizontal displacement $\overline{u}$, a non-dimensional displacement λ can be calculated. First fiber breakage is observed for a horizontal displacement $\overline{u} = 139.96$ mm (Fig. 32), which corresponds to a non-dimensional displacement $\lambda = 0.976$. By comparing Figs. 32 and 33, the model correctly predicts the location of fiber breakage. The "generalized" (because of the introduction of damage) numerical model fits well the force-displacement curve throughout the experiment, up to the onset of fiber breakage (Fig. 34).

In Ref. [58], pivot damage due to shear, i.e., fibers detaching due to friction in pivots, is taken into account, thereby allowing for sliding between the two families of fibers. Thus, the nonlinear homogenized quasi-static model for the discrete system in Fig. 11 (for more details about the homogenization procedure the reader is

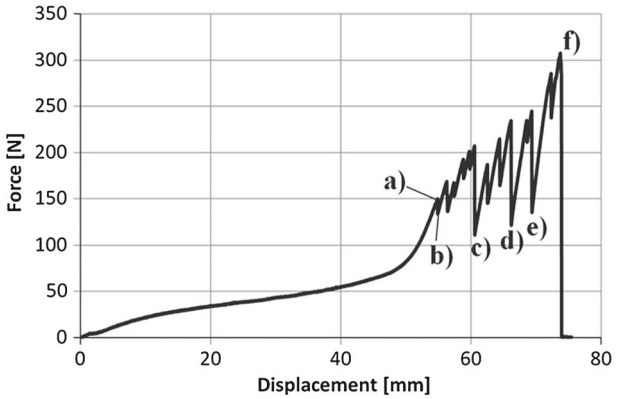

Fig. 31 Force versus prescribed displacement for a uniaxial bias extension test. **a** Sample before first beam breakage (i.e., breakdown onset); **b** upper-left corner beam breakage; **c**–**f** further fiber breakage

Fig. 32 **a** Reference configuration ($\lambda = 0$), **b** damage onset ($\lambda = 0.976$) of a shear test

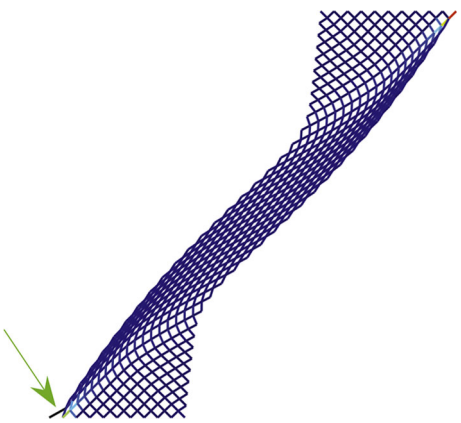

Fig. 33 Deformed configuration at the onset of damage. The broken fiber is colored in black, and it is pointed by the green arrow (color figure online)

referred to Ref. [13]) is modified by introducing, in the spirit of mixture theory, two independent placement functions χ^1 and χ^2 (the placement functions of body points belonging to horizontal and vertical fibers, respectively) defined on the same reference domain and, accordingly, considering the following nonlinear (elastic) strain energy to be minimized at each iteration

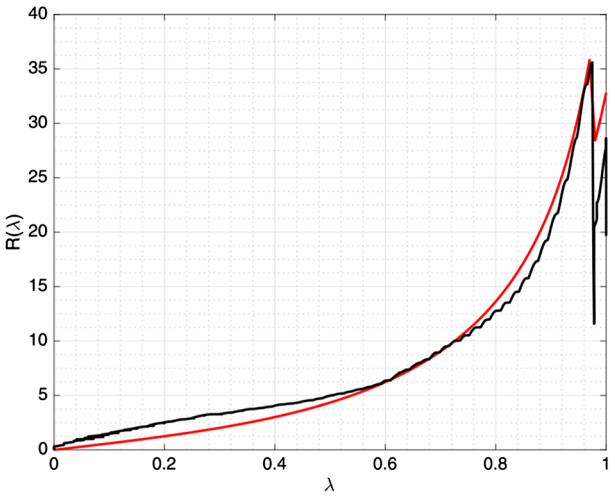

Fig. 34 Force (N) versus non-dimensional displacement for the shear test of a pantographic sheet up to the onset of fiber breakage. The black curve is the experimental data, and the red curve has been obtained via numerical simulation (color figure online)

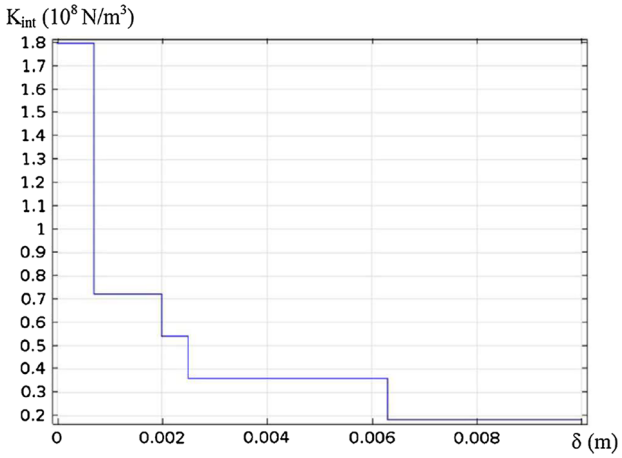

Fig. 35 Dependence of the resistance to sliding K_{int} on δ

$$\int_{\mathcal{B}_0} \underbrace{\sum_{\alpha=1,2} \frac{K_e^\alpha}{2} \|F^\alpha \hat{e}_\alpha - 1\|^2}_{\text{extension of horiz. and vert. fibers}} + \int_{\mathcal{B}_0} \underbrace{\frac{K_p}{2} \left| \arccos\left(\frac{F^1\hat{e}_1 \cdot F^2\hat{e}_2}{\|F^1\hat{e}_1\| \cdot \|F^2\hat{e}_2\|} \right) - \frac{\pi}{2} \right|^\xi}_{\text{shear (pivots torsion) contribution}} + \tag{44}$$

$$\int_{\mathcal{B}_0} \underbrace{\sum_{\alpha=1,2} \frac{K_b^\alpha}{2} \left[\frac{\|\nabla F^\alpha | \hat{e}_\alpha \otimes \hat{e}_\alpha\|^2}{\|F^\alpha \hat{e}_\alpha\|^2} - \left(\frac{F^\alpha \hat{e}_\alpha \cdot \nabla F^\alpha | \hat{e}_\alpha \otimes \hat{e}_\alpha}{\|F^\alpha \hat{e}_\alpha\|^2} \right)^2 \right]}_{\text{bending of horiz. and vert. fibers}} + \int_{\mathcal{B}_0} \underbrace{\frac{K_{\text{int}}}{2} \|\chi^1 - \chi^2\|^2}_{\text{relative sliding of the two layers}} \tag{45}$$

In Ref. [58], the relative sliding of two families of fibers is considered. A criterion based on thresholds for the relative distance $\delta = \|\chi^1 - \chi^2\|$ between χ^1 and χ^2 (e.g., the fitted K_{int} in Fig. 35) is presented.

A numerical example where an aluminum specimen is subject to uniaxial bias extension is shown. Constitutive parameters K_e^α, K_b^α, K_p and K_{int} were fitted using experimental data (Fig. 36), showing a very good agreement. The experiment is studied only up to the first rupture (i.e., as long as $K_{\text{int}} > 0 \; \forall X \in \mathcal{B}_0$). For the discrete model [57], and in turn for the continuum homogenized model [58] (as for their respective purely elastic counterparts), it is straightforward to implement the case of non-orthogonal initially straight fibers [60].

Further, the two models have been extensively tested when dealing with pure (nonlinear) elasticity, and they show a nearly perfect agreement with experimental results. In Fig. 37b, the onset of damage is observed at the

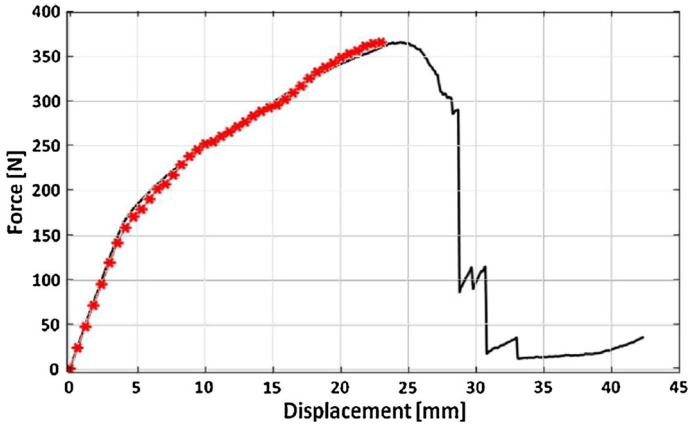

Fig. 36 Force versus applied displacement for a uniaxial bias extension test of an aluminum pantographic sheet. The black curve is the experimental measurement and the red obtained via numerical simulation (color figure online)

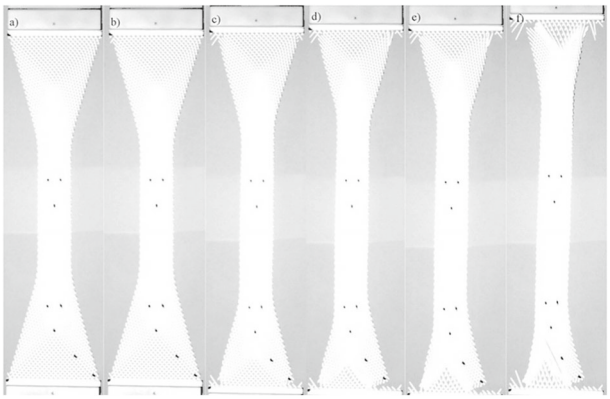

Fig. 37 A sample subject to uniaxial bias extension. **a** Sample before the first beam breakage (i.e., breakdown onset); **b** upper-left corner beam rupture; **c**–**f** rupture of further fibers

upper-left corner beam only. This is due to undesired asymmetries in the experimental setup (e.g., specimen, loading, clamping).

3 Feasibility of digital image correlation analyses

Up to now, the only reported kinematic data were prescribed macro-displacements or discrete measurements (e.g., control angles, see Fig. 17). In the future, it is desirable to have a richer experimental database in order to calibrate and validate in a more thorough way the previously discussed models. Since very large displacement levels occur, digital image correlation (DIC [61,62]) is a natural choice for the measurement technique. The feasibility of DIC on pantographic samples was shown very recently [63]. In that case study, a series of 30 load steps was analyzed with global DIC using meshes made of 3-noded triangles with linear shape functions (i.e., T3-DIC). Since the mesh was not compatible with the pantograph mesostructure, elastic regularization was used (i.e., so-called RT3-DIC [64]). In order to avoid any significant bias, the regularization length was identical to the element length (i.e., 25 pixels).

This example is further analyzed hereafter. Figure 38 shows the initial configuration, the last configuration prior to damage inception (i.e., 30th load step), and the broken sample. The grips were speckled for DIC purposes, and the hinges of the pantographic sheet were marked in black. A red background was used in order to create high contrast with the white color of pantographic sheet.

The first type of analysis consists in meshing the rectangular region of interest with T3 elements independently of the underlying mesostructure [63]. Such discretizations may then be compared with numerical simulations performed at the macroscale (as discussed above). Three different mesh densities are considered

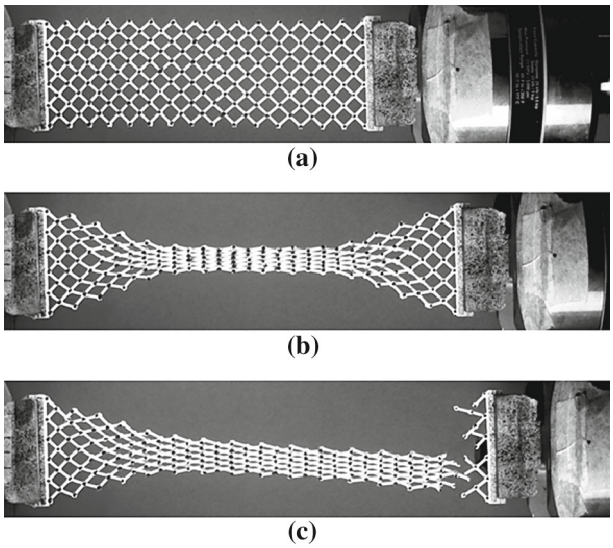

Fig. 38 Gray-level images of the pantograph in the reference configuration (**a**), last analyzed deformed configuration (**b**), and at failure (**c**)

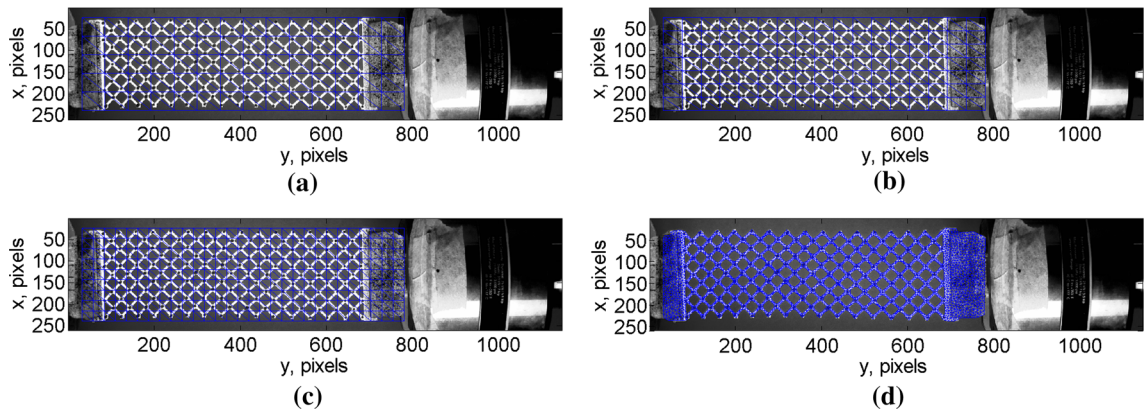

Fig. 39 Finite element meshes overlaid with the gray-level picture of the reference configuration

(Fig. 39a–c). The characteristic mesh size $\overline{\ell}$, which is defined as the square root of the average element surface, is equal to 34 pixels for the first mesh, 28 pixels for the second one, and 18 pixels for the third. Second, a fourth mesh was tailored to the pantograph surface (Fig. 39d). Thanks to the uniform background, simple morphological operations were performed in order to construct this mesoscale mesh from a mask. The characteristic mesh size is equal to 3.5 pixels.

Two types of registration routes are followed, namely the first one is an incremental approach that consists in updating the reference configuration that becomes the deformed configuration of the previous analysis. Its main advantage is that the elastic regularization only acts incrementally (i.e., equivalent to a hyperelastic description with Hencky strains). The convergence condition on the norm of the mean displacement correction was set to 10^{-3} pixel. The regularization length was selected to be equal to 45 pixels in that case. This choice enables the second, third and fourth meshes to be analyzed even though they are finer than the underlying mesostructure. The drawback is that measurement uncertainties are cumulated as more pictures are analyzed. A second option is to perform direct calculations that register the nth picture with that of the reference (i.e., unloaded) configuration. The measurement uncertainties are no longer cumulated. However, the elastic regularization may become too strong for the actual kinematics as it acts as a low-pass filter. Consequently, the regularization length was lowered to 30 pixels. The convergence condition on the norm of the mean displacement correction was set to 10^{-2} pixel since the measured displacement amplitudes will be significantly higher than in incremental registrations.

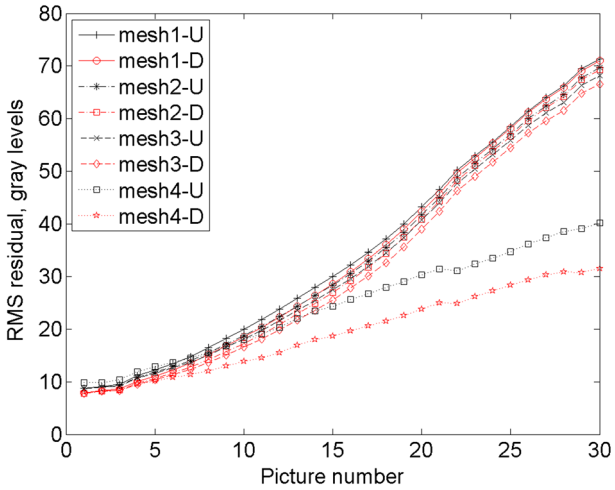

Fig. 40 RMS residual as a function of the picture number for the four meshes shown in Fig. 39. The extension U corresponds to updated registrations, and the extension D designates direct registrations

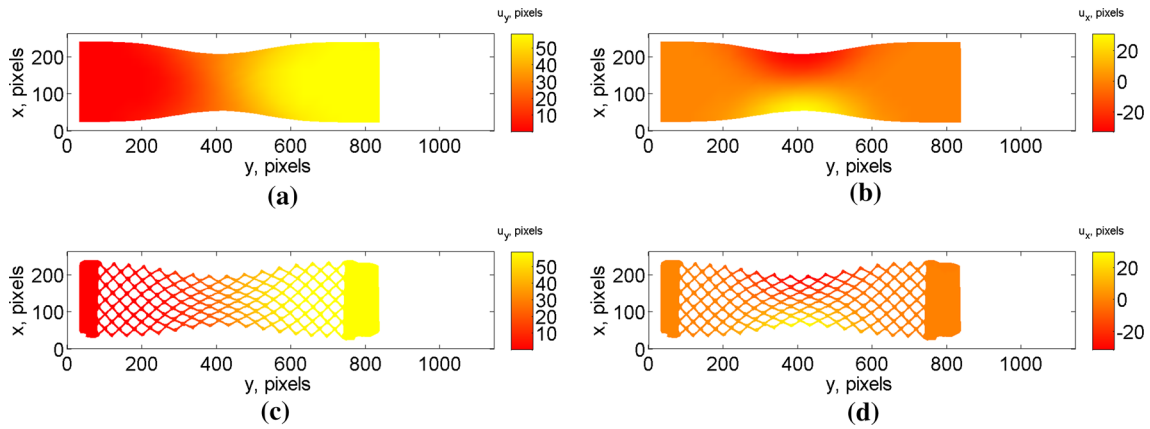

Fig. 41 Longitudinal (**a**–**c**) and transverse (**b**–**d**) displacement fields measured with meshes 3 (**a**, **b**) and 4 (**c**, **d**) for the 10th picture. The fields are shown on the deformed configuration

In T3-DIC, the quality of the registration is probed with the gray-level residual field, namely the pixelwise difference between the picture in the reference configuration and the picture in the deformed configuration corrected by the measured displacement field. The root-mean-square (RMS) average is reported in Fig. 40 for all eight situations considered herein. The first general trend is that the registration quality degrades as more steps are analyzed, thereby signaling that the measured fields do not fully capture the complex kinematics associated with the studied pantograph at the end of the experiment. Second, the direct registrations have always lower levels in comparison with updated registrations. This result validates the choice of the regularization strategy. Last, there is a clear difference between the first three meshes and the last one. This proves that a mesh tailored to the actual pantograph surface is able to better capture the kinematics of the test, even with the same regularization length as for the coarser meshes. In terms of measurement quality, the three meshes lead to similar overall residuals, which is to be expected because the regularization length is larger than the element size. For mesh 4, the gain between direct and updated registration is the highest.

In the following discussion, only two sets of results are reported, namely those of meshes 3 and 4 for direct registrations. Figure 41 shows the longitudinal and transverse displacements measured for the 10th picture. The transverse displacement field u_x shows that there is a huge contraction, which is of the order of magnitude as the longitudinal motions u_y. Given the fact that the width of the sample is one-third of its length, it proves that transverse deformations are much more important than the longitudinal component. This is due to the geometry of the pantographic sheet. The same observation applies for both meshes. In the present case, both measurements have approximately the same quality in terms of overall registration residuals (Fig. 40).

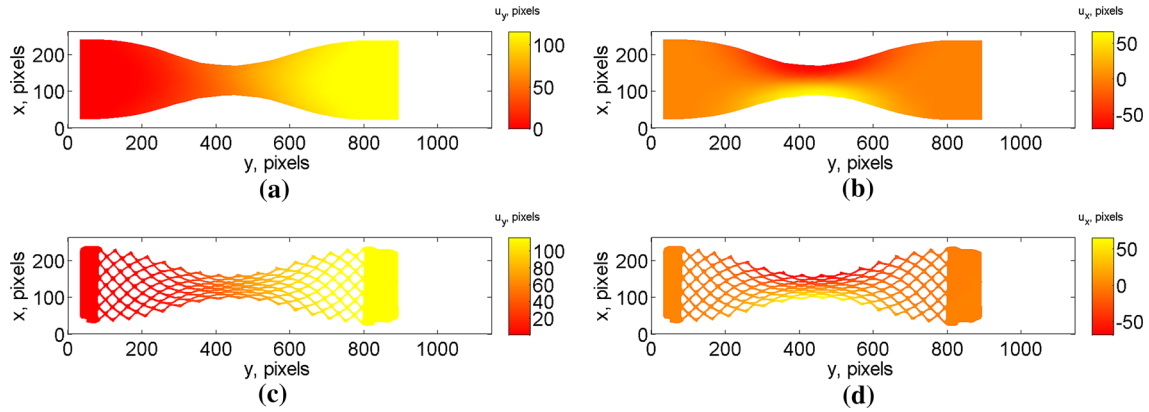

Fig. 42 Longitudinal (**a**–**c**) and transverse (**b**–**d**) displacement fields measured with meshes 3 (**a**, **b**) and 4 (**c**, **d**) for the 20th picture. The fields are shown on the deformed configuration

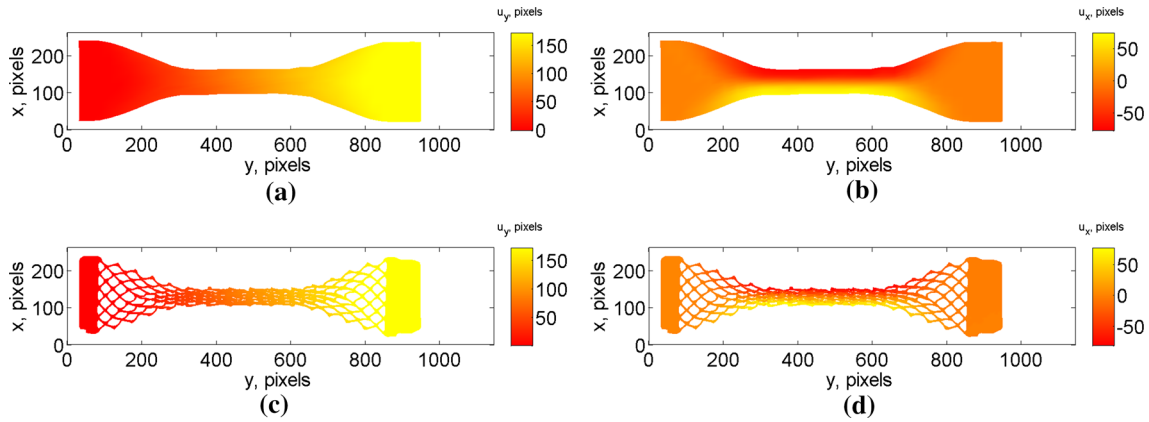

Fig. 43 Longitudinal (**a**–**c**) and transverse (**b**–**d**) displacement fields measured with meshes 3 (**a**, **b**) and 4 (**c**, **d**) for the 30th picture. The fields are shown on the deformed configuration

In Fig. 42, the same fields are shown for the 20th picture. The pattern of the transverse and longitudinal displacement fields is very similar with higher overall levels. The displacement ranges still are of the same order of magnitude for the longitudinal and transverse displacements. Consequently, the central part of the sample has become even thinner. The kinematic details are more easily observed for mesh 4. In this case, there is a clearer difference that translates into lower registration residuals for mesh 4 (Fig. 40).

The last load level prior to damage inception (i.e., first strut failure) is reported in Fig. 43. In that case, the gray-level residuals (Fig. 40) are significantly higher for mesh 3 in comparison with mesh 4. In both cases, the chosen kinematic basis is no longer able to completely describe the actual motions of the pantographic structure. For the parts of the pantographic sheet closer to the grips and the grips themselves, the registration quality is significantly better. This result validates the choice of including part of the speckled grips in the analysis. For this last step, the highly deformed region has grown toward both ends of the pantographic sheet, which can be understood by the fact that when struts touch each other, the deformation mechanism moves away from these zones.

The results reported herein show that DIC analyses can be run on pantographic structures at macroscopic *and* mesoscopic levels. Significant gains were observed in terms of registration quality by moving from the macroscopic to the mesoscopic scale (i.e., more than a factor of two at the end of the picture series). However, the final gray-level residuals indicate that even more refined approaches should be followed. What is missing in the mesoscopic analysis is the fact that pivots were not accounted for. This would require meshes to be constructed in such a way that the actual geometry of the pantographic structures would be described. Two options are possible. The first one would consist in using beam elements that are interconnected at the pivots. DIC analyses may then be easier since the number of degrees of freedom would be significantly reduced [65]. Second, instead of using beam elements, finite elements may also be considered with explicit descriptions

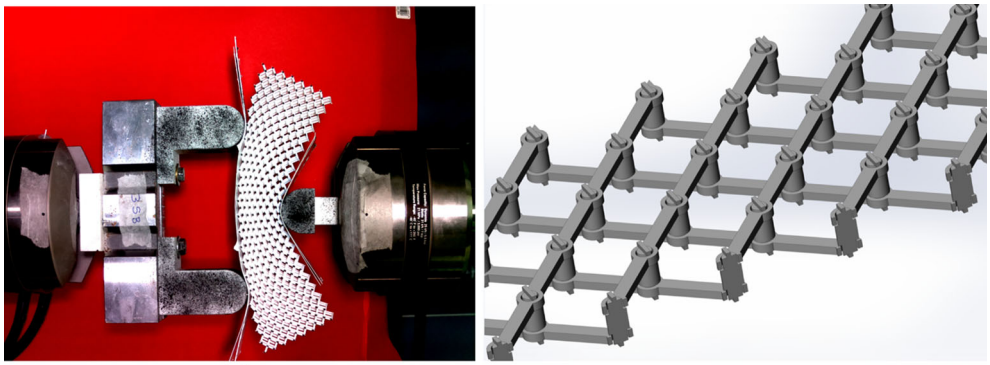

(a) **(b)**

Fig. 44 **a** Three-point flexural test on a 3D pantographic specimen. **b** Pantographic sheet with "perfect" hinges

of the pivots (as in the 3D Cauchy model, see Fig. 20). One challenge is to measure surface displacements with such very fine meshes since each element will contain very few pixels. This approach requires elastic regularizations to be considered [64] as performed herein. Last, integrated approaches may also be considered in which the displacement fields are derived thanks to numerical simulations and the material parameters then become the unknowns. In that case, the mesh can be as fine as wished since the number of unknowns has been drastically reduced [66,67].

4 Conclusion and outlook

Pantographic fabrics proved to be a very interesting subject of study, involving the work of, at least, (computational) mechanicians (modeling), experimentalists (experiments), numerical analysts (model solving), data analysts (image correlation), mathematicians (well-posedness and Γ-convergence) and many other researchers and professionals. We believe that what has been presented in this survey can thus be considered our manifesto about how commitment from different groups of researchers should be directed for the study of metamaterials and, more generally, for the study of every scientific subject. Mechanics, as any other natural science, cannot proceed without a continuous interplay between experimental evidence and theoretical modeling.

However, this is just a first simple step toward the study of more complex structures and experiments. A famous quote by Hilbert states that "the art of doing mathematics consists in finding that special case which contains all the germs of generality." This statement can be extended to every scientific discipline, including those that have been applied in the studies presented in this survey and that pantographic fabrics can be considered as one of the simplest examples leading to treat nonstandard problems in mechanics of materials and its related disciplines. In this sense, pantographic structures provide the minimal setting for the study of relevant issues in mechanics. The solution of a general problem is easier to face once that of its particular cases has been addressed, as, very often, particular cases help to understand better the real nature of the problem. Currently, new tests and structures are being studied, along with their technological realization challenges, like the three-point test shown in Fig. 44a and the pantographic sheet with "perfect" pivots, i.e., hinges that do not oppose to variations of the shear angle between two intersecting fibers, shown in Fig. 44b.

Acknowledgements This work was supported by a grant from the Government of the Russian Federation (contract No. 14.Y26.31.0031).

References

1. dell'Isola, F., Steigmann, D., Della Corte, A.: Synthesis of fibrous complex structures: designing microstructure to deliver targeted macroscale response. Appl. Mech. Rev. **67**(6), 060804 (2015)
2. Milton, G., Briane, M., Harutyunyan, D.: On the possible effective elasticity tensors of 2-dimensional and 3-dimensional printed materials. Math. Mech. Complex Syst. **5**(1), 41–94 (2017)
3. Eremeyev, V.A., Pietraszkiewicz, W.: Material symmetry group and constitutive equations of micropolar anisotropic elastic solids. Math. Mech. Solids **21**(2), 210–221 (2016)
4. Bertram, A., Glüge, R.: Gradient materials with internal constraints. Math. Mech. Complex Syst. **4**(1), 1–15 (2016)

5. Russo, L.: The Forgotten Revolution: How Science Was Born in 300 BC and Why It Had to Be Reborn. Springer, Berlin (2013)
6. Stigler, S.M.: Stigler's law of eponymy. Trans. N. Y. Acad. Sci. **39**(1 Series II), 147–157 (1980)
7. dell'Isola, F., Andreaus, U., Placidi, L.: At the origins and in the vanguard of peridynamics, non-local and higher-gradient continuum mechanics: an underestimated and still topical contribution of Gabrio Piola. Math. Mech. Solids **20**(8), 887–928 (2015)
8. dell'Isola, F., Corte, A.D., Giorgio, I.: Higher-gradient continua: the legacy of Piola, Mindlin, Sedov and Toupin and some future research perspectives. Math. Mech. Solids **22**(4), 852–872 (2017)
9. Del Vescovo, D., Giorgio, I.: Dynamic problems for metamaterials: review of existing models and ideas for further research. Int. J. Eng. Sci. **80**, 153–172 (2014)
10. dell'Isola, F., Lekszycki, T., Pawlikowski, M., Grygoruk, R., Greco, L.: Designing a light fabric metamaterial being highly macroscopically tough under directional extension: first experimental evidence. Z. angew. Math. Phys. **66**, 3473–3498 (2015)
11. Alibert, J.-J., Seppecher, P., dell'Isola, F.: Truss modular beams with deformation energy depending on higher displacement gradients. Math. Mech. Solids **8**(1), 51–73 (2003)
12. Pideri, C., Seppecher, P.: A second gradient material resulting from the homogenization of an heterogeneous linear elastic medium. Contin. Mech. Thermodyn. **9**(5), 241–257 (1997)
13. dell'Isola, F., Giorgio, I., Pawlikowski, M., Rizzi, N.: Large deformations of planar extensible beams and pantographic lattices: heuristic homogenization, experimental and numerical examples of equilibrium. Proc. R. Soc. A **472**(2185), 23 (2016)
14. dell Isola, F., Seppecher, P., Della Corte, A.: The postulations á la d alembert and á la cauchy for higher gradient continuum theories are equivalent: a review of existing results. In: Proceedings of the Royal Society A, Volume 471, p. 20150415. The Royal Society (2015)
15. Auffray, N., dell'Isola, F., Eremeyev, V., Madeo, A., Rosi, G.: Analytical continuum mechanics à la Hamilton–Piola least action principle for second gradient continua and capillary fluids. Math. Mech. Solids **20**(4), 375–417 (2015)
16. Altenbach, H., Eremeyev, V.: On the linear theory of micropolar plates. ZAMM **89**(4), 242–256 (2009)
17. Pietraszkiewicz, W., Eremeyev, V.: On natural strain measures of the non-linear micropolar continuum. Int. J. Solids Struct. **46**(3), 774–787 (2009)
18. Rahali, Y., Giorgio, I., Ganghoffer, J.F., dell'Isola, F.: Homogenization à la piola produces second gradient continuum models for linear pantographic lattices. Int. J. Eng. Sci. **97**, 148–172 (2015)
19. Bilotta, A., Formica, G., Turco, E.: Performance of a high-continuity finite element in three-dimensional elasticity. Int. J. Numer. Methods Biomed. Eng. **26**(9), 1155–1175 (2010)
20. Cazzani, A., Malagù, M., Turco, E.: Isogeometric analysis: a powerful numerical tool for the elastic analysis of historical masonry arches. Contin. Mech. Thermodyn. **28**(1–2), 139–156 (2016)
21. de Saint-Venant, M.: Mémoire sur la torsion des prismes: avec des considérations sur leur flexion ainsi que sur l'équilibre intérieur des solides élastiques en général: et des formules pratiques pour le calcul de leur résistance à divers efforts s' exerçant simultanément. Imprimerie nationale (1856)
22. Mindlin, R.D., Tiersten, H.F.: Effects of couple-stresses in linear elasticity. Arch. Ration. Mech. Anal. **11**(1), 415–448 (1962)
23. Dillon, O.W., Perzyna, P.: Gradient theory of materials with memory and internal changes. Arch. Mech. **24**(5–6), 727–747 (1972)
24. Abdoul-Anziz, H., Seppecher, P.: Strain gradient and generalized continua obtained by homogenizing frame lattices (2017) . <hal-01672898>
25. Turco, E., Giorgio, I., Misra, A., dell'Isola, F.: King post truss as a motif for internal structure of (meta) material with controlled elastic properties. Open Sci. **4**(10), 171153 (2017)
26. Everstine, G.C., Pipkin, A.C.: Boundary layers in fiber-reinforced materials. J. Appl. Mech. **40**, 518–522 (1973)
27. Hilgers, M.G., Pipkin, A.C.: Elastic sheets with bending stiffness. Q. J. Mech. Appl. Math. **45**, 57–75 (1992)
28. Hilgers, M.G., Pipkin, A.C.: Energy-minimizing deformations of elastic sheets with bending stiffness. J. Elast. **31**, 125–139 (1993)
29. Hilgers, M.G., Pipkin, A.C.: Bending energy of highly elastic membranes ii. Q. Appl. Math. **54**, 307–316 (1996)
30. Hu, M.Z., Kolsky, H., Pipkin, A.C.: Bending theory for fiber-reinforced beams. J. Compos. Mater. **19**, 235–249 (1985)
31. Pipkin, A.C.: Generalized plane deformations of ideal fiber-reinforced materials. Q. Appl. Math. **32**, 253–263 (1974)
32. Pipkin, A.C.: Energy changes in ideal fiber-reinforced composites. Q. Appl. Math. **35**, 455–463 (1978)
33. Pipkin, A.C.: Some developments in the theory of inextensible networks. Q. Appl. Math. **38**, 343–355 (1980)
34. dell'Isola, F., d'Agostino, M.V., Madeo, A., Boisse, P., Steigmann, D.: Minimization of shear energy in two dimensional continua with two orthogonal families of inextensible fibers: the case of standard bias extension test. J. Elast. **122**(2), 131–155 (2016)
35. Placidi, L., Greco, L., Bucci, S., Turco, E., Rizzi, N.L.: A second gradient formulation for a 2d fabric sheet with inextensible fibres. Z. angew. Math. Phys. **67**(5), 114 (2016)
36. Rivlin, R.S.: Plane strain of a net formed by inextensible cords. In: Collected Papers of RS Rivlin, pp. 511–534. Springer (1997)
37. Greco, L., Giorgio, I., Battista, A.: In plane shear and bending for first gradient inextesible pantographic sheets: numerical study of deformed shapes and global constraint reactions. Math. Mech. Solids, p. 1081286516651324 (2016)
38. Cuomo, M., Dell'Isola, F., Greco, L., Rizzi, N.L.: First versus second gradient energies for planar sheets with two families of inextensible fibres: investigation on deformation boundary layers, discontinuities and geometrical instabilities. Compos. B Eng. **115**, 423–448 (2017)
39. Cuomo, M., dell'Isola, F., Greco, L.: Simplified analysis of a generalized bias test for fabrics with two families of inextensible fibres. Z. angew. Math. Phys. **67**(3), 1–23 (2016)
40. dell'Isola, F., Cuomo, M., Greco, L., Della Corte, A.: Bias extension test for pantographic sheets: numerical simulations based on second gradient shear energies. J. Eng. Math. **103**(1), 127–157 (2017)

41. Greco, L., Giorgio, I., Battista, A.: In plane shear and bending for first gradient inextensible pantographic sheets: numerical study of deformed shapes and global constraint reactions. Math. Mech. Solids **22**(10), 1950–1975 (2017)
42. Giorgio, I.: Numerical identification procedure between a micro-cauchy model and a macro-second gradient model for planar pantographic structures. Z. angew. Math. Phys. **67**(4), 95 (2016)
43. Turco, E., dell'Isola, F., Cazzani, A., Rizzi, N.L.: Hencky-type discrete model for pantographic structures: numerical comparison with second gradient continuum models. Z. angew. Math. Phys. **67**, 28 (2016)
44. Eremeyev, V.A., dell'Isola, F., Boutin, C., Steigmann, D.: Linear pantographic sheets: existence and uniqueness of weak solutions (2017). https://doi.org/10.1007/s10659-017-9660-3
45. Placidi, L., Barchiesi, E., Turco, E., Rizzi, N.L.: A review on 2D models for the description of pantographic fabrics. Z. angew. Math. Phys. **67**(5), 121 (2016)
46. dell'Isola, F., Steigmann, D.J.: A two-dimensional gradient-elasticity theory for woven fabrics. J. Elast. **18**, 113–125 (2015)
47. Giorgio, I., Grygoruk, R., dell'Isola, F., Steigmann, D.J.: Pattern formation in the three-dimensional deformations of fibered sheets. Mech. Res. Commun. **69**, 164–171 (2015)
48. Giorgio, I., Rizzi, N.L., Turco, E.: Continuum modelling of pantographic sheets for out-of-plane bifurcation and vibrational analysis. Proc. R. Soc. A, p. 21 (2017). https://doi.org/10.1098/rspa.2017.0636
49. Auffray, N., Dirrenberger, J., Rosi, G.: A complete description of bi-dimensional anisotropic strain-gradient elasticity. Int. J. Solids Struct. **69**, 195–206 (2015)
50. Boutin, C., dell'Isola, F., Giorgio, I., Placidi, L.: Linear pantographic sheets: asymptotic micro–macro models identification. Math. Mech. Complex Syst. **5**(2), 127–162 (2017)
51. Placidi, L., Andreaus, U., Corte, A.D., Lekszycki, T.: Gedanken experiments for the determination of two-dimensional linear second gradient elasticity coefficients. Z. angew. Math. Phys. **66**(6), 3699–3725 (2015)
52. Placidi, L., Barchiesi, E., Battista, A.: An inverse method to get further analytical solutions for a class of metamaterials aimed to validate numerical integrations. In: Mathematical Modelling in Solid Mechanics, pp. 193–210. Springer (2017)
53. Scerrato, D., Zhurba Eremeeva, I.A., Lekszycki, T., Rizzi, N.L., Rizzi, N.L.: On the effect of shear stiffness on the plane deformation of linear second gradient pantographic sheets. ZAMM **96**(11), 1268–1279 (2016)
54. dell'Isola, F., Giorgio, I., Andreaus, U.: Elastic pantographic 2d lattices: a numerical analysis on static response and wave propagation. Proc. Est. Acad. Sci. **64**, 219–225 (2015)
55. dell'Isola, F., Della Corte, A., Giorgio, I., Scerrato, D.: Pantographic 2D sheets. Int. J. Non Linear Mech. **80**, 200–208 (2016)
56. Madeo, A., Della Corte, A., Greco, L., Neff, P.: Wave propagation in pantographic 2d lattices with internal discontinuities. arXiv preprint arXiv:1412.3926 (2014)
57. Turco, E., dell'Isola, F., Rizzi, N.L., Grygoruk, R., Müller, W.H., Liebold, C.: Fiber rupture in sheared planar pantographic sheets: numerical and experimental evidence. Mech. Res. Commun. **76**, 86–90 (2016)
58. Spagnuolo, M., Barcz, K., Pfaff, A., Dell'Isola, F., Franciosi, P.: Qualitative pivot damage analysis in aluminum printed pantographic sheets: numerics and experiments. Mech. Res. Commun. **83**, 47–52 (2017)
59. Ganzosch, G., dell'Isola, F., Turco, E., Lekszycki, T., Müller, W.H.: Shearing tests applied to pantographic structures. Acta Polytech. CTU Proc. **7**, 1–6 (2016)
60. Turco, E., Golaszewski, M., Giorgio, I., D'Annibale, F.: Pantographic lattices with non-orthogonal fibres: experiments and their numerical simulations. Compos. B Eng. **118**, 1–14 (2017)
61. Sutton, M.A., Orteu, J.J., Schreier, H.: Image Correlation for Shape, Motion and Deformation Measurements: Basic Concepts, Theory and Applications. Springer, Berlin (2009)
62. Hild, F., Roux, S.: Digital Image Correlation, pp. 183–228. Wiley-VCH, Weinheim (2012)
63. Turco, E., Misra, A., Pawlikowski, M., dell'Isola, F., Hild, F.: Enhanced piola-hencky discrete models for pantographic sheets with pivots without deformation energy: numerics and experiments (submitted for publication) (2018)
64. Tomičević, Z., Hild, F., Roux, S.: Mechanics-aided digital image correlation. J. Strain Anal. Eng. Des. **48**(5), 330–343 (2013)
65. Hild, F., Roux, S., Gras, R., Guerrero, N., Marante, M.E., Flórez-López, J.: Displacement measurement technique for beam kinematics. Opt. Lasers Eng. **47**(3), 495–503 (2009)
66. Leclerc, H., Périé, J.-N., Roux, S., Hild, F.: Integrated digital image correlation for the identification of mechanical properties. In: Gagalowicz, A., Philips, W. (eds.) International Conference on Computer Vision/Computer Graphics Collaboration Techniques and Applications, Volume LNCS 5496, pp. 161–171. Springer, Berlin (2009)
67. Lindner, D., Mathieu, F., Hild, F., Allix, O., Ha Minh, C., Paulien-Camy, O.: On the evaluation of stress triaxiality fields in a notched titanium alloy sample via integrated DIC. J. Appl. Mech. **82**(7), 071014 (2015)